Acta Materialia 97 (2015) 380–391

Contents lists available at ScienceDirect

Acta Materialia

journal homepage: www.elsevier.com/locate/actamat

Heat affected zone microstructures and their influence on toughness in two microalloyed HSLA steels

Bevis Hutchinson [a], Jacek Komenda [a], Gregory S. Rohrer [b], Hossein Beladi [c,*]

[a] SwereaKIMAB, Box 7047, Kista, SE-16407, Sweden
[b] Department of Materials Science and Engineering, Carnegie Mellon University, Pittsburgh, PA 15213-3890, USA
[c] Institute for Frontier Materials, Deakin University, Geelong, VIC 3216, Australia

ARTICLE INFO

Article history:
Received 14 March 2015
Revised 13 May 2015
Accepted 19 May 2015

Keywords:
Heat affected zone
Toughness
Bainite
Inter-variant plane distribution
EBSD

ABSTRACT

Microstructures and Charpy impact properties have been examined in two microalloyed steels following heat treatments to simulate weld heat affected zone (HAZ) structures over a range of heat input conditions, characterised by the cooling time from 800 to 500 °C ($\Delta t_{8/5}$). The base materials were low carbon structural steel plates microalloyed with vanadium and nitrogen (V–N) and niobium (Nb), respectively. The toughnesses of the HAZs displayed remarkably different behaviours as shown by their impact transition temperatures. For the V–N steel, the toughness improved with increasingly rapid cooling (low heat input conditions) whereas the Nb steel showed an opposite trend. Some of this behaviour could be explained by the presence of coarse ferrite grains in the slowly cooled V–N steel. However, other conditions where all the structures were bainitic and rather similar in optical micrographs gave widely different toughness values. The recently developed method of five dimensional boundary analysis based on electron backscattering diffraction has been applied to these cases for the first time. This showed that the lath boundaries in the bainite were predominantly on {1 1 0} planes of the ferrite and that the average spacing of these boundaries varied depending on steel composition and cooling rate. Since {1 1 0} is also the slip plane in ferrite, it is considered that close spacing between the lath boundaries inhibits general plasticity at stress concentrations and favours initiation of fracture. The differences between the two steels are believed to be due to their transformation behaviours on cooling where precipitation of vanadium nitride in austenite accelerates ferrite formation and raises the temperature of the phase transformation in V–N steels.

1. Introduction

Among the primary requirements of structural steels are good mechanical properties in connection with welding, notably toughness. In recent decades, great advances have been made through developments in steelmaking, with significant reductions in the contents of detrimental elements such as carbon, sulphur and phosphorus. At the same time, strength levels have increased so that resistance to fracture remains an important issue. The properties of the weld metal itself are possible to control through the use of consumables having suitably designed alloying additions but the heat affected zones adjacent to welds (HAZs) are often the most critical regions with regard to potential failures. Although the steel chemistry is not affected in the HAZ, exposure to very high temperature and variable cooling conditions give rise to microstructures that deviate widely from the ideal ones existing after controlled processing and are often undesirable with respect to toughness. When reviewing the situation of welding microalloyed steels, Hart [1] identified three main problem areas. These were (i) the existence of hard zones with the associated risk of hydrogen cracking, (ii) the toughness of coarse grained heat affected zones (CG HAZ) close to the fusion line, especially in the case of single pass welds and (iii) toughness of these CG HAZ when they have been exposed to reheating into the inter-critical temperature range (IC CG HAZ) in successive welding passes. The present work concentrates on the second of these, toughness of the CG HAZ and uses thermal treatments to simulate effects of welding heat.

A number of metallurgical factors are known to affect CG HAZ properties. Prior austenite grains close to the fusion line can become very large which may affect the toughness directly as well as through their effect on the nature and scale of transformation products in the microstructure after cooling. The cooling rate also controls the transformation products and this depends on the heat

* Corresponding author.
E-mail address: hossein.beladi@deakin.edu.au (H. Beladi).

http://dx.doi.org/10.1016/j.actamat.2015.05.055
1359-6454/

input that is used in relation to the thickness of the material being welded. Low heat input conditions lead to higher cooling rates, often specified in terms of the time for cooling through the transformation range from 800 to 500 °C, $\Delta t_{8/5}$. Microalloying of steels with aluminium, vanadium, niobium or titanium generally has a favourable influence since carbide and nitride particles help to restrain austenite grain growth, especially TiN [2]. These elements also assist in binding up 'free' nitrogen which is known to have a deleterious influence on toughness [3]. Steel specifications are typically more tolerant with respect to nitrogen content in microalloyed than in plain steels, e.g., [4]. Nevertheless, different steel chemistries can lead to very different results of HAZ properties depending on the welding conditions and, in particular, the heat input parameter. Where possible, it is desirable to employ low heat input welding for economy, minimised distortion and a better working environment as, for example, in newer welding methods such as laser, laser-hybrid and pulsed arc processes [5,6].

Very high heat input welding generally has a deleterious effect on HAZ toughness because the slow cooling rates, e.g., $\Delta t_{8/5} > 100$ s, give rise to coarse grained ferrite-pearlite microstructures. The situation with regard to low and medium heat inputs seems to be more complex, especially in the case of V-microalloyed steels where higher nitrogen contents are normally used to maximise the strengthening effect of vanadium [7]. Several reports [7–11] have shown that HAZ toughness of V-steels or V–Nb-steels with low nitrogen contents ($N < \sim 0.005\%$) is not very sensitive to heat input conditions in this range. However, with higher nitrogen levels ($N > \sim 0.008\%$) there appears to be a transition from inferior toughness for higher heat inputs to superior toughness for lower, with the transition occurring in the vicinity of $\Delta t_{8/5} \sim 30$ s. Work by Zajac et al. [7,9] showed that the reduced toughness in the HAZ of V–N-microalloyed steels following slower cooling could be associated with coarse pro-eutectoid ferrite grains lining the prior austenite grain boundaries. For this reason, the fracture surfaces sometimes gave an impression of intergranular cleavage failure. However, the cause of high toughness in other situations could not be assigned. The main aim of the present work was to investigate this phenomenon in more detail, to extend the measurements to faster cooling conditions appropriate to some modern welding processes, and to use detailed metallographic examinations to better understand the relationships between HAZ microstructures and toughness.

2. Experimental procedure

The present work was carried out on two commercially manufactured plates of HSLA steels, one coded A with V–N microalloying and the other, D, containing Nb. Their chemical compositions are given in Table 1. Steel A was provided as 6 mm strip manufactured via a thin slab casting route while steel D was a 10 mm product from a conventional hot strip mill. In order to make the comparison as valid as possible, both steels were milled to 5 mm and this dimension was used in sub-size Charpy tests. Because of their small size, the absolute values of impact energy cannot be regarded as valid; however, their relative behaviours, depending on steel chemistry and weld simulation conditions, are believed to be meaningful. Before heat treatment the specimens were nickel-plated to restrict oxidation and decarburization. Weld HAZ simulation was carried out in a custom-made Joule heating facility. Temperatures were measured using very thin thermocouples (0.1 mm wires) spot-welded in the middle of the specimens and these were used to programme the heating and cooling cycles. The cycles involved heating at 100 °C/s to 1350 °C, holding for 2 s and then cooling at prescribed rates through the temperature range from 800 to 500 °C corresponding to $\Delta t_{8/5}$ times of 2, 10, 20 and 40 s. The specimens were then notched according to the Charpy-V standard and tested at different temperatures. The Charpy results typically refer to either two or three specimens for a given testing temperature. Other specimens from both steels having cylindrical form, φ 3 mm × 10 mm, were examined in a Bähr 805A/D dilatometer following the same thermal cycle in order to observe the transformation behaviour during cooling. For simplicity, the steel and heat treatments are combined in a single identification so that, for example, D2 means steel D with a cooling time of 2 s.

Hardness measurements were made on the HAZ regions and their microstructures were examined by optical microscopy and by advanced scanning electron microscopy using electron back-scattering diffraction (EBSD). The optical microscopy was performed on specimens etched by 2% nital. The EBSD measurements were conducted by a field emission gun Quanta 3D FEI scanning electron microscope operated at 20 kV and 4 nA. The instrument was equipped with a fully automated EBSD device attachment. Data acquisition and post processing were conducted by the TexSEM Laboratories, Inc. software (TSL). Multiple EBSD maps were acquired using a spatial step size of 0.2 μm on a hexagonal grid for all heat treatment simulations. Extra maps with a step size of 0.5 μm were also conducted in one case for steel D to measure the mean spacing of inter-variant boundary network. An automated stereological procedure [12] was used in the present study to measure the inter-variant boundary character distribution of the ferrite laths using the EBSD data collected for each heat treatment condition.

3. Results and discussion

Apart from their microalloy contents the steel chemistries are quite similar, with D having slightly higher carbon and manganese levels. As is normally the case, the steel D microalloyed with Nb has a low nitrogen content of 0.004% whereas the V-steel contains more nitrogen at 0.014%. Both steels are rather similar in strength in the as-received conditions so, as potential competitor materials, their response to welding makes an interesting comparison. Values of Vickers hardness after the different weld HAZ simulations are presented in Fig. 1. Steel D is somewhat harder than A after each similar treatment, probably a consequence of its slightly greater C and Mn contents. The cooling rate has a greater influence and the hardness in both materials tends to become less with slower cooling, increasing $\Delta t_{8/5}$, as expected.

Results of Charpy energies normalised to a fracture area of 1 cm^2 are presented in Fig. 2(a)–(d) for the different HAZ simulation conditions. There was a considerable scatter in the values which is not uncommon in these types of measurements due to the coarse prior austenite grain sizes and also exacerbated in the present case by the rather small specimen sizes used here. However, the trends appear to be quite consistent.

Table 1
Chemical compositions of the two steels in this investigation in wt.%.

Steel	C %	Mn %	Si %	S	P	Al %	N %	V %	Nb %
A	0.059	0.87	0.03	0.004	0.008	0.034	0.014	0.076	0.010
D	0.065	1.37	0.01	0.002	0.016	0.041	0.0038	0.010	0.041

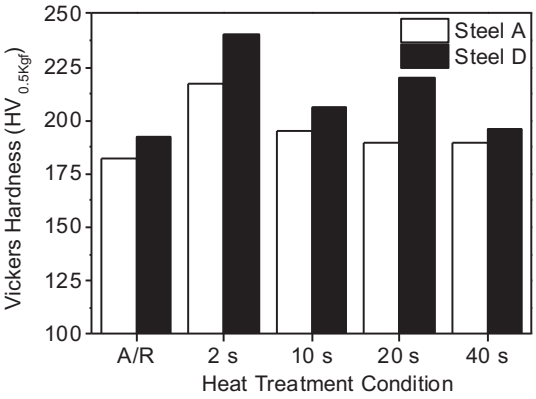

Fig. 1. Hardness values for the steels in as-received condition and after heat treatment with different cooling times $\Delta t_{8/5}$.

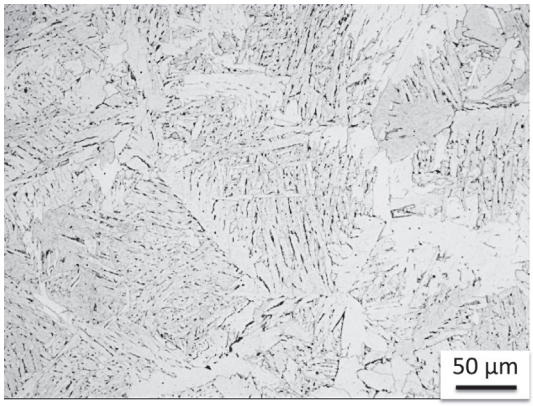

Fig. 3. Optical micrograph of steel A after weld simulation with cooling time $\Delta t_{8/5}$ of 40 s.

The upper shelf energies are broadly similar for both steels and all heat treatment conditions but there are marked differences in the ductile to brittle transition range. For the slowest cooling conditions the Nb-microalloyed steel D shows considerably lower transition temperatures. Perhaps surprising is the tendency for this steel to show improving toughness behaviour for slower cooling rates all the way from $\Delta t_{8/5}$ of 2 to 40 s. It would normally be expected that this trend would reverse on even slower cooling as the microstructure becomes increasingly coarse. The V–N microalloyed steel A shows an opposite trend with improvement of toughness as the cooling rate increases with longer $\Delta t_{8/5}$ times. The same behaviour has been observed previously [7,9] and was attributed to formation of large polygonal ferrite grains delineating the austenite grain boundaries. The same phenomenon was confirmed in the present case as can be seen in Fig. 3 with ferrite grains up to 100 µm in length formed along the prior austenite grain boundaries. Below the transition temperature, cleavage cracks have been seen permeating these large ferrite grains and the macroscopic fracture surface gives an impression of intergranular cleavage cracks in a network on the scale of the austenite grain size. These effects have been well documented previously [7] so the rest of this paper will concentrate on the newer results pertaining to the rapid cooling conditions of low energy welding and the origin of the high toughness in the V–N microalloyed steel.

The behaviours for the steels and cooling conditions are summarised in Fig. 4 where the 40 J impact transition temperatures are plotted as a function of the cooling time $\Delta t_{8/5}$. Evidently, the scatter in the Charpy impact data affects the reliability of these ITT values but the general trends are indisputable. The two steels, which are quite similar apart from their microalloying, show strikingly different behaviours. In particular, the V–N steel A has its best toughness for the cooling time of 2 s corresponding to the most

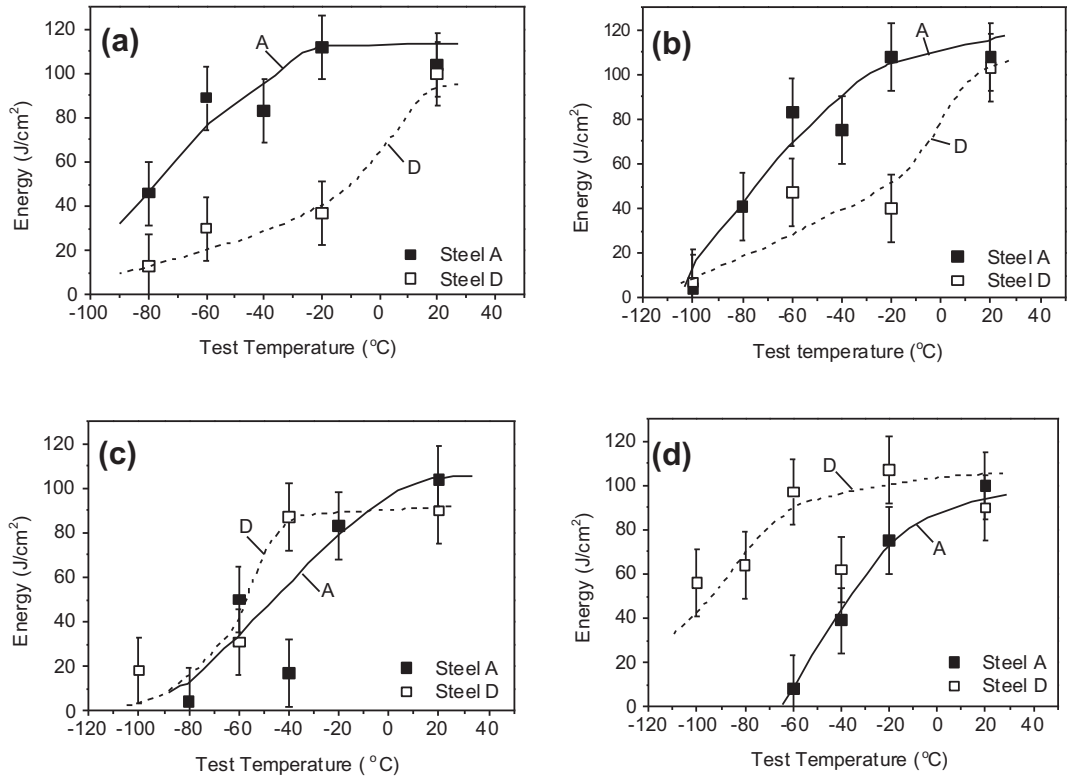

Fig. 2. Charpy energy curves for the simulated HAZ structures having cooling times $\Delta t_{8/5}$ of (a) 2 s, (b) 10 s, (c) 20 s and (d) 40 s.

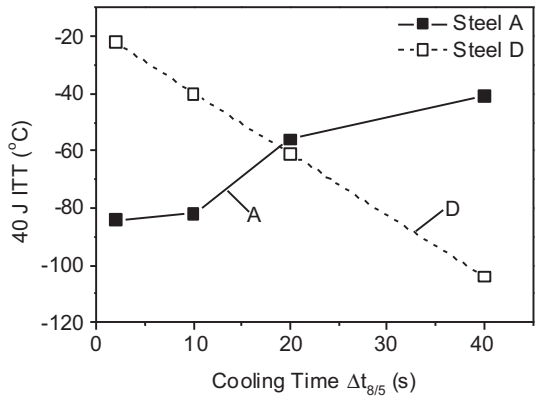

Fig. 4. Impact transition temperatures for steels A and D after weld simulation with different cooling times $\Delta t_{8/5}$.

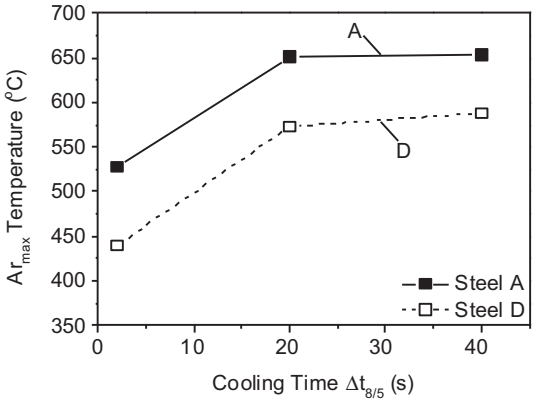

Fig. 6. Results of dilatometry showing the temperatures at the fastest rate of phase transformation for steel A (V–N) and steel B (Nb) during cooling at different rates, as cooling times $\Delta t_{8/5}$.

rapid cooling whereas the Nb steel D is, on the contrary, best following slow cooling. Comparison of the results in Fig. 4 with the hardness values in Fig. 1 shows no correlation so the toughness behaviour is not simply related to differences in the plastic flow stress of the steels. Furthermore, a deleterious influence from free nitrogen is not a logical explanation since the nitrogen should be most completely combined as VN or AlN following slow cooling. Any possible detrimental effect of nitrogen should, therefore, occur with rapid cooling yet this is just the condition where steel A exhibits its best toughness. The sulphur contents of both steels were very low (Steel A 0.004%S and steel D 0.002%S). These alone would not be expected to cause significant differences in the toughness of the two steels. We believe the toughness to be dependent on microstructural features that require more detailed description as will be presented below. Before that, however, it is relevant to consider some aspects of the phase transformations on cooling that were obtained from dilatometer experiments. Thermal cycles similar to those used for the Charpy specimens were repeated in the dilatometer. Examples of curves with the fastest cooling rates of 150 °C/s from 1350 °C, corresponding to $\Delta t_{8/5}$ of 2 s, for both steels are shown in Fig. 5.

It can be seen that the start and finish of transformation from austenite to ferrite are both significantly higher in steel A than in steel D and so is the temperature at which the change occurs most rapidly. This last condition, corresponding to the temperature for the fastest rate of transformation, is plotted for three different cooling rates in Fig. 6 where there is seen to be a displacement of some 80° between the steels. The shift is virtually the same for start and finish temperatures and also for all cooling conditions ($\Delta t_{8/5}$). It is well known that the ferrite microstructure is controlled principally by the temperature of the phase transformation so the difference seen here can be expected to relate directly to the measured variations in toughness.

Steel chemistry is well known to affect the temperature for the start of transformation and various relationships have been reviewed [13] giving e.g.

$$Ae_3 = 910 - 203\sqrt{\%C} + 29\%Si - 10.7\%Mn, \text{ and}$$
$$Ae_3 = 871 - 255\%C + 19\%Si - 11\%Mn$$

Although somewhat different in formulation, applying both these to the present cases shows that the differences in chemistry between steels A and D can account for only about 9° difference in transformation temperature and so most of the discrepancy (~70°) cannot be due to the base compositions. A similar behaviour was observed previously when comparing two V-microalloyed steels having different nitrogen contents of 0.003% and 0.013% [7]. The higher nitrogen steel transformed at temperatures that were about 70 °C above the lower one and similar behaviour is also clearly evident in published CCT transformation diagrams [14] comparing steels with comparable low and high nitrogen contents. It is remarkable that higher nitrogen levels in V-steels give rise to much higher transformation temperatures despite the fact that nitrogen is an austenite stabiliser and so should induce the opposite effect in an equilibrium situation. It therefore seems probable that the large influence of steel chemistry seen here originates in the combination of vanadium and nitrogen in steel A, although it should also be noted that the present Ar_3 temperatures during cooling are considerably lower than the equilibrium Ae_3 values in both cases.

The most plausible explanation for these effects at present is based on the knowledge that vanadium nitride particles can act as nucleants for ferrite during cooling [15] and so accelerate its

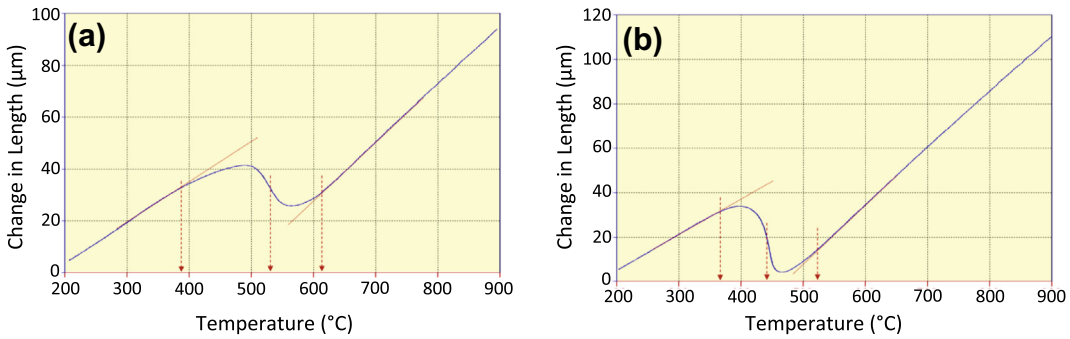

Fig. 5. Dilatometer curves for (a) steel A and (b) steel D for cooling at 150 °C/s from 1350 °C, $\Delta t_{8/5}$ equal to 2 s.

formation with a concomitant rise in the transformation temperature. At the peak temperature of welding or, as here, of simulation, the vanadium will all be dissolved in the austenite. On cooling, there will not be sufficient time for precipitation of VN inside the austenite grains but this may occur at the grain boundaries at lower temperatures prior to the phase transformation. When this happens, the VN particles can accelerate the usual process of ferrite nucleation, raising the transformation temperature as observed. During slower cooling, the ferrite grains have time to grow excessively which is detrimental. However, on faster cooling, very fine networks of polygonal ferrite nucleated at VN particles in the austenite grain boundaries may interfere with the subsequent transformation to bainite. Such an effect of prior ferrite on interference with the bainite reaction was reported in a recent publication by Zhu et al. [16].

Optical microscopy showed that the microstructure were very homogeneous for each condition. The steels contained bainitic microstructures after rapid cooling. Both had coarse prior austenite grains (PAGs); for steel A the mean PAG intercept length was approximately 75 μm while for steel D it was somewhat larger at around 120 μm. Individual austenite grains could be much larger, up to 300 μm in D. Otherwise, it was difficult to specify evident differences between the two steels, all being dominated by acicular microstructures with fine cementite particles distributed between the laths. Optical micrographs in Fig. 7 show structures in three interesting cases. Steels A and D with $\Delta t_{8/5} = 2$ s (Fig. 7a and b) appear to be rather similar yet these two cases deviate greatly in toughness with a difference of some 50 °C in their impact transition temperatures. Steel D with $\Delta t_{8/5} = 40$ s (Fig. 7c) has a coarser lath structure but its toughness is akin to that of the material in Fig. 7a. Narrow ferrite grains or films are visible along some of the PAG boundaries in these latter two cases but not in Fig. 7b.

In view of the limited scope offered by optical microscopy, it was decided to examine the lath-like microstructures using advanced SEM–EBSD methods that have been developed in recent years [12]. Briefly, the method provides a statistical measure of the frequency of different interfaces in terms of their five degrees of freedom. Three of these refer to the misorientation of the adjacent crystal lattices and the other two define the plane of the lath boundary. This method has addressed various fundamental aspects of grain boundaries in metals and ceramics (e.g., [17–22]) but the present work is perhaps the first time that it has been applied to a notable technological problem. Details of the EBSD maps are summarised in Table 2 for all conditions. Due to the very low carbon content in steels, ~0.06 wt.%, the crystal structure can be assumed to be body centred cubic (bcc) for all heat treatment conditions [23]. Some further details are given in Appendix A.

Table 2
EBSD measurement conditions for different heat treatment profiles.

Heat treatment condition	Step size (μm)	EBSD area	Line segments
Steel A2	0.2	$250 \times 250\ \mu m^2 \times 4$	~62,000
Steel D2	0.2	$250 \times 250\ \mu m^2 \times 3$	~78,000
Steel D40	0.2	$250 \times 250\ \mu m^2 \times 14$	~50,000
Steel D40	0.5	$470 \times 470\ \mu m^2 \times 3$	–

The number of line traces/segments after excluding the boundary segments of less than 0.6 μm are summarised in Table 2 for all heat treatment conditions. These line traces/segments were used to measure the five-parameter boundary character distribution. In the present study, the analysis was performed at 9 bins per 90° level of discretization, having about 10° resolution (i.e., 97% of the bins contained at least ten observations). Further details are given in the Appendix A.

3.1. The inter-variant interface/boundary character distribution

'Variants' here refers to the different orientations of ferrite laths in the bainite that derive from a single prior austenite grain. An automated stereological procedure was used in the present study to measure the inter-variant boundary character distribution using the EBSD data collected for each heat treatment condition [12]. In this process, the boundary traces/segments are defined against the lattice misorientation and orientation inside the section plane. This procedure mainly requires an adequate number of boundary traces, i.e., the intersection lines between a boundary plane (here

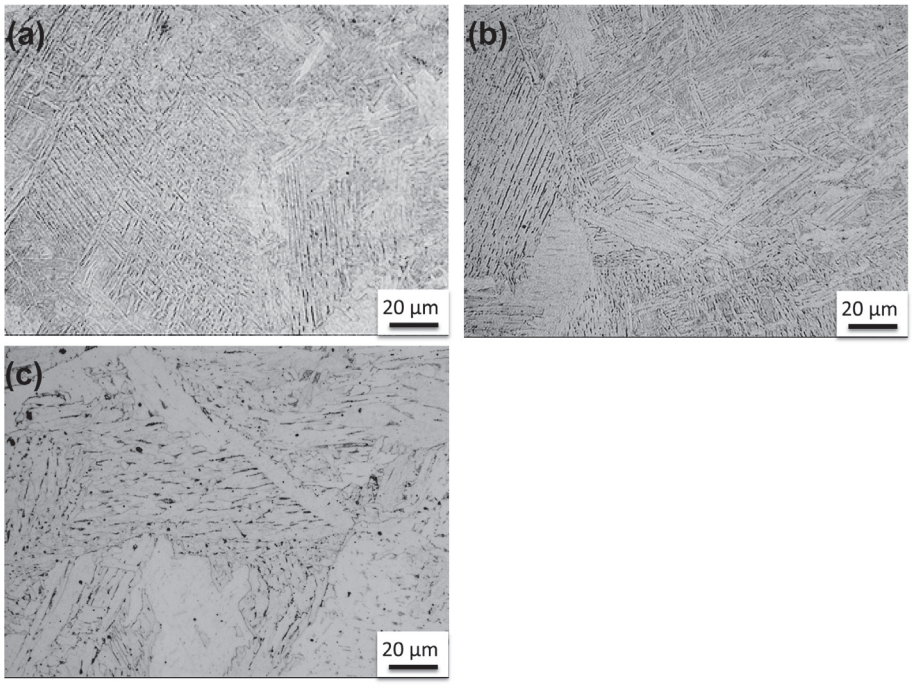

Fig. 7. Optical micrographs of structures in (a) Steel A, $\Delta t_{8/5} = 2$ s, (b) Steel D, $\Delta t_{8/5} = 2$ s and (c) Steel D, $\Delta t_{8/5} = 40$ s.

two adjacent interface variants/laths) and the surface (i.e., plane of observation). Even though it is not realistic to resolve the actual plane orientation for a given trace, the plane is required to locate in the zone of the trace. Hence, collecting a sufficient number of traces (e.g., more than 50,000 boundary traces for a cubic system [12]) from the EBSD data makes it possible to determine statistically the orientation of a given boundary/interface plane. The distribution of boundary character is the relative areas of distinguishable boundaries described by their lattice misorientation and the orientation of their boundary plane. It is measured in multiples of a random distribution (MRD), where the values greater than one mean that planes were observed more frequently than expected in a random distribution.

3.2. Mean spacing of inter-variant boundary network

An automated software was developed to display the grain boundaries in an EBSD map as a function of disorientation angle

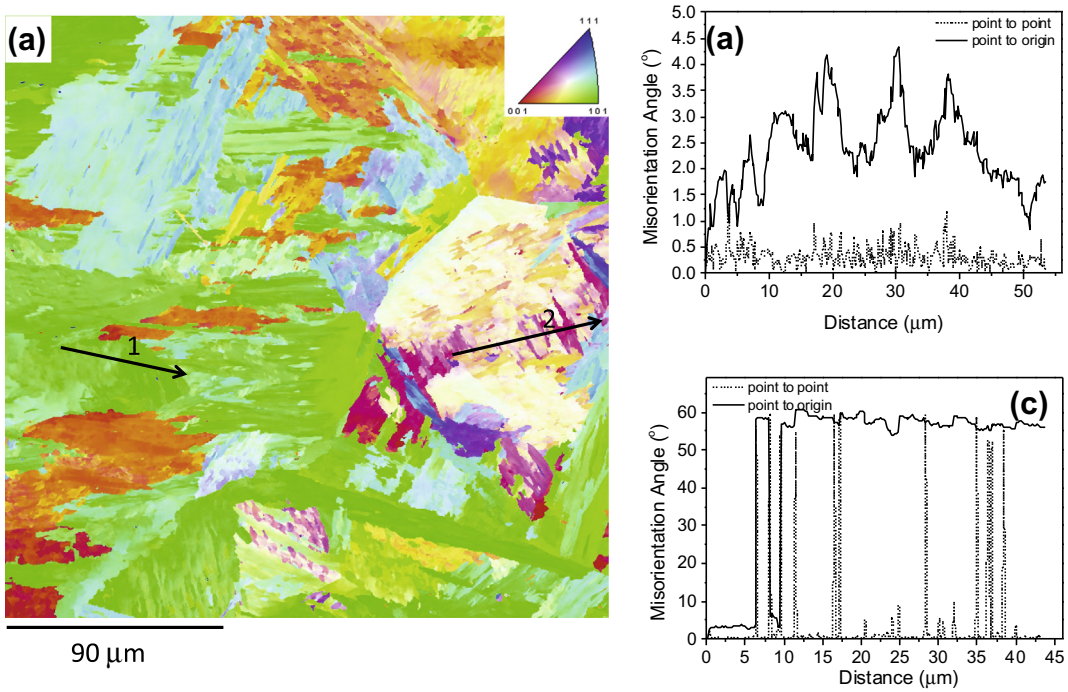

Fig. 8. (a) IPF map for steel D40. Misorientation angle profile along (b) arrow 1, (c) arrow 2 (b) shown in (a). Inset in (a) represents the colour codes referred to normal direction. (For interpretation of the references to colour in this figure legend, the reader is referred to the web version of this article.)

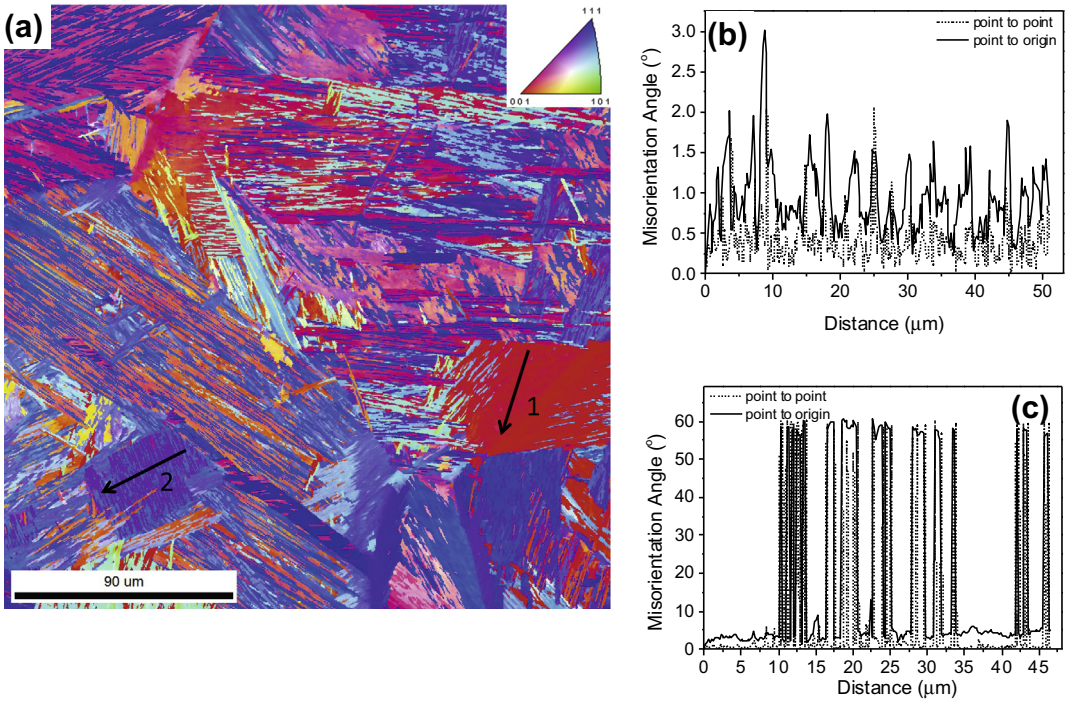

Fig. 9. (a) IPF map for steel D2. Misorientation angle profiles along (b) arrow 1, (c) arrow 2 shown in (a). Inset in (a) represents the colour codes referred to normal direction. (For interpretation of the references to colour in this figure legend, the reader is referred to the web version of this article.)

and/or axis. The high reheating temperature of 1350 °C resulted in very coarse prior austenite grain size of 200–300 μm, significantly enhancing the hardenability of steels. The microstructure of steel D40 was mostly bainitic structure containing very coarse blocks of bainite (~50 μm), consisting of parallel laths with similar orientation having misorientation angles in the range of 0.2–4° (Fig. 8). Occasionally, fine blocks (i.e., ~10 μm) were also observed in the microstructure, separated by a misorientation angle ranging from ~10° to 60° (Fig. 8c). By contrast, the microstructure of steel D2 was dominated by very fine bainitic laths as small as 3 μm, mostly separated by a misorientation angle of 60°. Coarse blocks were also sometimes observed in steel D2 microstructure (Fig. 9). In steel A2, the microstructure consisted of a very small fraction of polygonal ferrite together with lath bainite. The size of the bainitic blocks varied significantly, ranging from 2 to ~60 μm (Fig. 10).

3.3. Inter-variant plane character distribution analysis

The misorientation angle distribution was qualitatively similar for all heat treatment conditions, revealing a bimodal distribution with two peaks at low (~10–15°) and high (~50–60°) misorientation angle ranges (Fig. 11). However, the steel D2 revealed a much stronger peak at ~60° and a relatively weaker one at low misorientations in comparison with steels A2 and D40, probably associated with the presence of a much finer bainitic microstructure.

In theory, a given prior austenite grain can potentially transform into 12 or 24 different orientations/variants, depending on the orientation relationship between the parent austenite and transformed product (e.g., bainite). Here, it was assumed that the orientation relationship is, on average, close to the Young–Kurdjumov–Sachs [24,25] (Y–K–S) for the current study. Therefore, each prior austenite grain can potentially give rise to 24 different variants, resulting in 16 independent misorientation angle/axis pairs due to symmetry, as listed in Table 3. The presence of a bimodal misorientation profile in all cases was closely associated with the theoretical inter-variant misorientation angles for the Y–K–S condition (Table 3). The intermediate misorientation angle populations, approximately in the range of 20–40°, can be referred to misorientation angles inherited from the prior austenite grain boundaries (Fig. 11).

The 24 theoretical variants resulting from the Y–K–S relationships can be divided into four distinct crystallographic packets in a given prior austenite grain, where each individual packet has laths sharing the same parallel ferrite plates, as the habit plane (e.g., V1–V6 in Table 3). In the steel D2, most inter-variant boundary populations were related to the variants (i.e., bainitic laths) from the same crystallographic packet (Fig. 12b). Among all

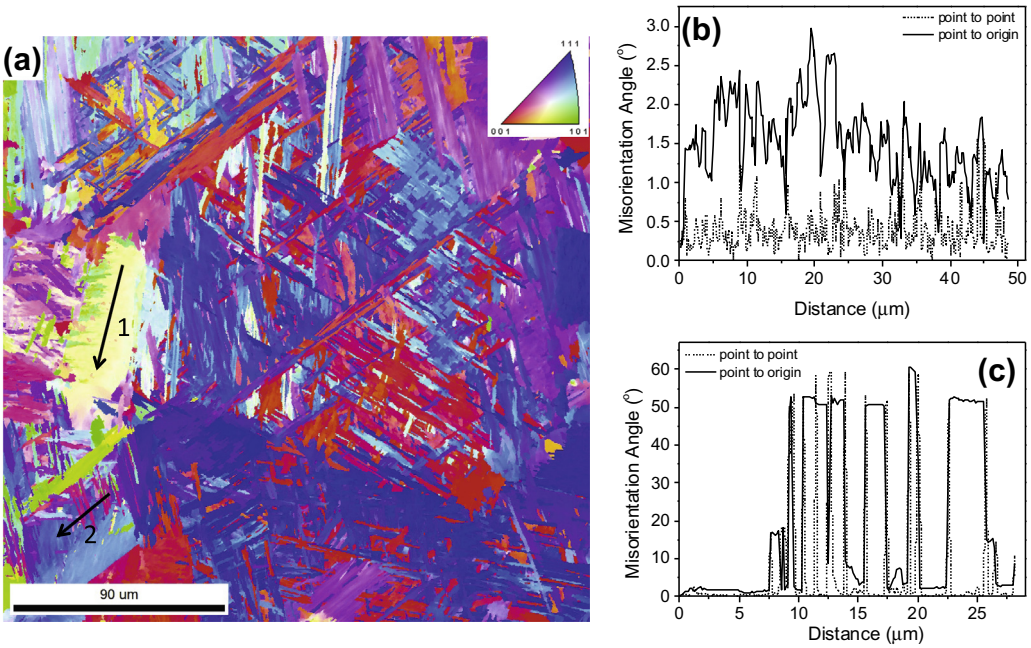

Fig. 10. (a) IPF map for steel A2. Misorientation angle profiles along (b) arrow 1, (c) arrow 2 shown in (a). Inset in (a) represents the colour codes referred to normal direction. (For interpretation of the references to colour in this figure legend, the reader is referred to the web version of this article.)

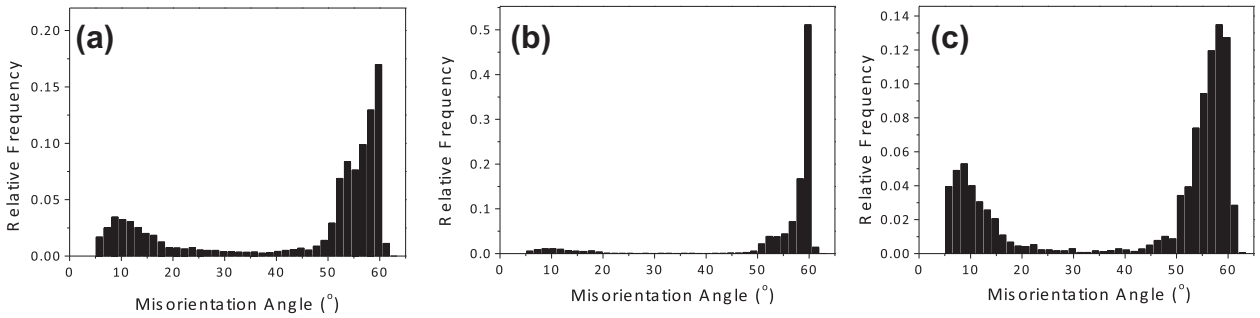

Fig. 11. Misorientation angle distribution for (a) steel A2, (b) steel D2, (c) steel D40.

Table 3
possible 24 variants generated through phase transformation having the Y–K–S orientation relationship.

Variant	Plane parallel	Direction parallel	Rotation angle/axis from V1
V1	$(111)_\gamma \parallel (011)_\alpha$	$[-101]_\gamma \parallel [-1-11]_\alpha$	–
V2		$[-101]_\gamma \parallel [-11-1]_\alpha$	60°/[11−1]
V3		$[01-1]_\gamma \parallel [-1-11]_\alpha$	60°/[011]
V4		$[01-1]_\gamma \parallel [-11-1]_\alpha$	10.5°/[0−1−1]
V5		$[1-10]_\gamma \parallel [-1-11]_\alpha$	60°/[0−1−1]
V6		$[1-10]_\gamma \parallel [-11-1]_\alpha$	49.5°/[011]
V7	$(1-11)_\gamma \parallel (011)_\alpha$	$[10-1]_\gamma \parallel [-1-11]_\alpha$	49.5°/[−1−11]
V8		$[10-1]_\gamma \parallel [-11-1]_\alpha$	10.5°/[11−1]
V9		$[-1-10]_\gamma \parallel [-1-11]_\alpha$	50.5°/[−103−13]
V10		$[-1-10]_\gamma \parallel [-11-1]_\alpha$	50.5°/[−7−55]
V11		$[011]_\gamma \parallel [-1-11]_\alpha$	14.9°/[1351]
V12		$[011]_\gamma \parallel [-11-1]_\alpha$	57.2°/[−356]
V13	$(-111)_\gamma \parallel (011)_\alpha$	$[0-11]_\gamma \parallel [-1-11]_\alpha$	14.9°/[5−13−1]
V14		$[0-11]_\gamma \parallel [-11-1]_\alpha$	50.5°/[−55−7]
V15		$[-10-1]_\gamma \parallel [-1-11]_\alpha$	57.2°/[−6−25]
V16		$[-10-1]_\gamma \parallel [-11-1]_\alpha$	20.6°/[11−11−6]
V17		$[110]_\gamma \parallel [-1-11]_\alpha$	51.7°/[−116−11]
V18		$[110]_\gamma \parallel [-11-1]_\alpha$	47.1°/[−24−1021]
V19	$(11-1)_\gamma \parallel (011)_\alpha$	$[-110]_\gamma \parallel [-1-11]_\alpha$	50.5°/[−31310]
V20		$[-110]_\gamma \parallel [-11-1]_\alpha$	57.2°/[36−5]
V21		$[0-1-1]_\gamma \parallel [-1-11]_\alpha$	20.6°/[30−1]
V22		$[0-1-1]_\gamma \parallel [-11-1]_\alpha$	47.1°/[−102124]
V23		$[101]_\gamma \parallel [-1-11]_\alpha$	57.2°/[−2−5−6]
V24		$[101]_\gamma \parallel [-11-1]_\alpha$	21.1°/[9−40]

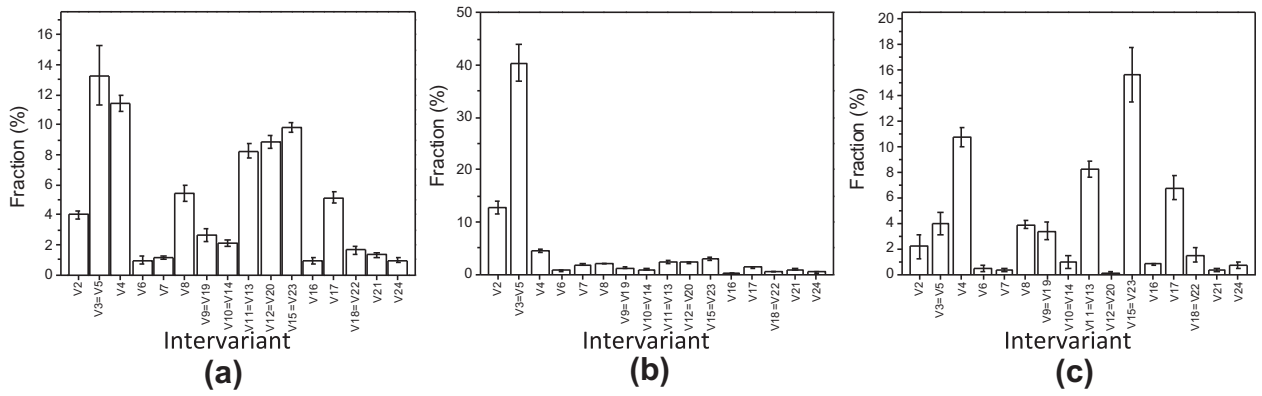

Fig. 12. Fraction of total populations of interfaces that belong to the Y–K–S condition, comparing inter-variant interfaces between V1 and V*i* (*i* = 2–24) for (a) steel A2, (b) steel D2 and (c) steel D40. Because of symmetry, there are only 16 independent inter-variant interface types, symbol = indicates two equivalent inter-variant interfaces.

interfaces in the steel D2, the V1–V6 inter-variant boundary represented a relatively small fraction despite belonging to the same crystallographic packet. The highest population with a fraction of 40% was for the V1–V3 inter-variant interfaces (i.e., 60°/[011]). On the contrary, for the steel D40, the most frequently observed inter-variant interfaces belonged to those formed as a result of the intersection of two different crystallographic packets (e.g., V1–V15 and V1–V11, Fig. 12c). For those interfaces in steel D40 associated with the same crystallographic packet, the V1–V4 interface (i.e., 10.5°/[0−1−1]) had the highest population at ~11% and the V1–V6 interface only showed ~4%. Interestingly, the inter-variant interface fraction belonging to the Y–K–S condition in steel A2 did not show any specific trend, revealing relatively similar fractions for most inter-variant interfaces (Fig. 12a). In A2, the total inter-variant interfaces resulting from the intersection of two laths within the same crystallographic packet (i.e., V1–V*i*, *i* = 2–6) was ~30% of the population, as compared to ~60% in D2 and ~17% for D40, respectively.

The distribution of inter-variant planes for all misorientations were qualitatively similar for all heat treatment conditions, showing strong anisotropy with pronounced maxima at the (101) positions (Fig. 13). The maximum was centred at the (101) position for all conditions with a value of 1.98, 2.06 and 1.55 MRD for steels A2, D2 and D40, respectively. In other words, the population of boundary planes on (101) was, for example, 98% greater than expected in a random distribution for steel A2. The minima of the distributions were centred on (100) for all conditions with

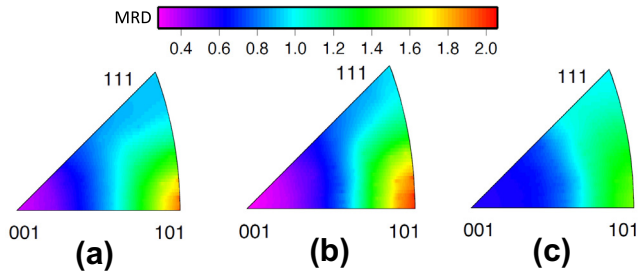

Fig. 13. Distribution frequencies in MRD for boundary plane summed over all misorientation angles (a) steel A2, (b) steel D2 and (c) steel D40.

0.35, 0.28 and 0.59 MRD for steels A2, D2 and D40, respectively (Fig. 13). Plane distributions parallel to (1 1 1) position showed approximately unity for all steels.

The inter-variant plane distributions for specific misorientation angle/axis pairs associated with the Y–K–S condition, listed in Table 3, were computed for all heat treatment conditions using the five macroscopic boundary parameters (Figs. 14–16). In general, the distribution of inter-variant planes varied significantly as a function of misorientation, although the distribution characteristics were qualitatively similar for specific misorientation angle/axis pair in all heat treatment conditions. Fig. 14 shows the inter-variant plane distributions about the [1 1 1] misorientation axis as a function of misorientation angle for all heat treatment conditions. For the 10.5° misorientation, the distributions have multiple peaks mainly centred on the zone axis of the tilt boundaries (i.e., the great circle perpendicular to [1 1 −1] or [−1 −1 1] axes in Fig. 14a). Twist boundaries also appeared in steel D40, though they were mostly absent in steels A2 and D2, as evident from the minimum intensity at their (1 1 −1) twist boundary position, Fig. 14a. The peak distributions were weakened from ~14 MRD at 10.5° to ~10 MRD at 49.5°, Fig. 14a and b. The distributions were mainly concentrated at the {1 1 0}||{1 1 0} symmetric tilt boundary positions (i.e., having the same surfaces on either side of the boundary) for all heat treatment conditions, the maximum being most pronounced for the steel A2. The {1 1 0} symmetric tilt boundary peaks dominated at the misorientation angle of 60°, with populations of ~43, ~107 and ~23 MRD for steels A2, D2 and D40, respectively (Fig. 14c).

The inter-variant plane distributions about the [1 0 1] misorientation axis showed a qualitatively similar development with

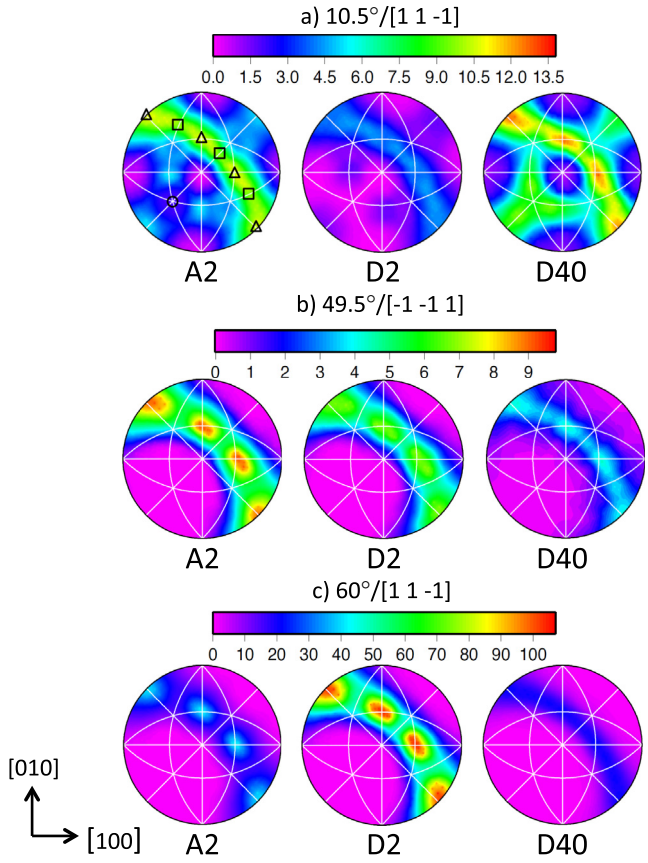

Fig. 14. Distributions of plane normals for boundaries having different misorientations with [1 1 −1] axes for steels A2, D2 and D40. Squares and triangles represent the positions of {1 1 2} and {1 1 0} symmetric tilt boundaries. The circle marks the location for {1 1 1} twist boundaries.

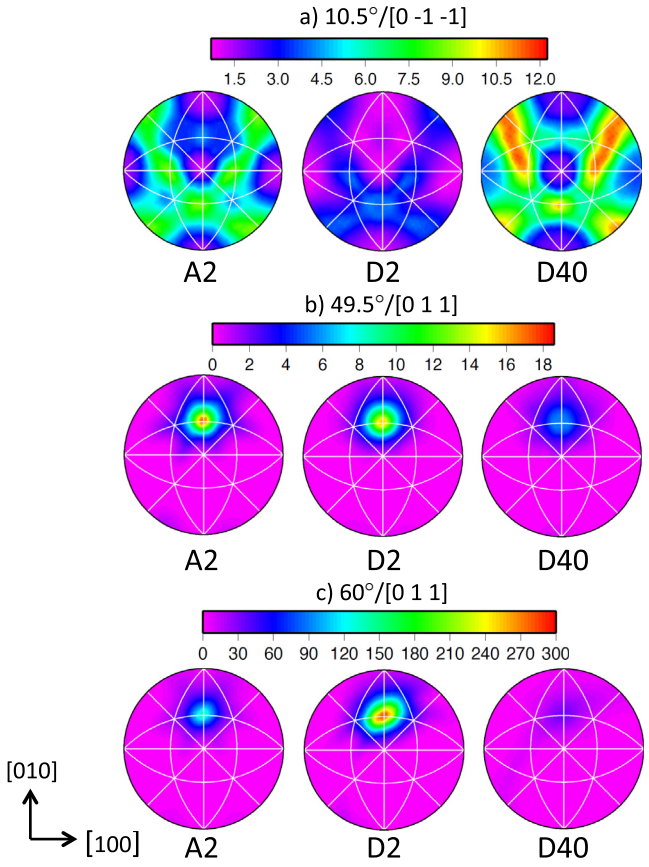

Fig. 15. Distributions of plane normals for boundaries in steels A2, D2 and D40 having different misorientations around [1 1 0] axis.

respect to the misorientation angle for all heat treatment conditions (Fig. 15). Multiple maxima appeared at different {1 1 0} positions for a misorientation of 10.53° in all cases, the highest population belonging to steel D40 with ~12 MRD (Fig. 15a). At the next misorientation angle of 49.5°, the distribution changed significantly with only a single peak at the twist boundary position of {1 1 0}||{1 1 0}. Except for the steel D40, the peaks strengthened, to approximately 19 and 17 MRD for steels A2 and D2, respectively (Fig. 15b). The distribution characteristics did not change at 60° for any of the conditions, although the populations were considerably increased at the (0 1 1) twist boundary position to about 148, 300 and 35 MRD for steels A2, D2 and D40, respectively (Fig. 15c).

The distribution of inter-variant planes for other high index misorientations listed in Table 3 typically revealed either one peak or multiple peaks approximately centred at or near the {1 1 0} plane positions (Fig. 16). The inter-variant plane distributions of these high index misorientations did not show any twist or tilt character, although it is possible that they had tilt or twist character in some other representation [26]. The relative population of boundaries with high index misorientations were mostly small compared with [1 1 0] and [1 1 1] misorientations. Some cases were significantly populated, however, especially those having a misorientation angle greater than 50.5° (Fig. 15).

When polycrystalline materials evolve by normal grain growth, there is an inverse relationship between the relative areas of grain boundary planes and their relative energies [18,20]. However, because the grain boundary plane distribution in the present material developed by transformation, the present results are expected to differ from those observed in other materials with bcc structure whose microstructures developed by grain growth (e.g., polygonal ferrite) [17,18]. The distribution of interface/boundary normals at

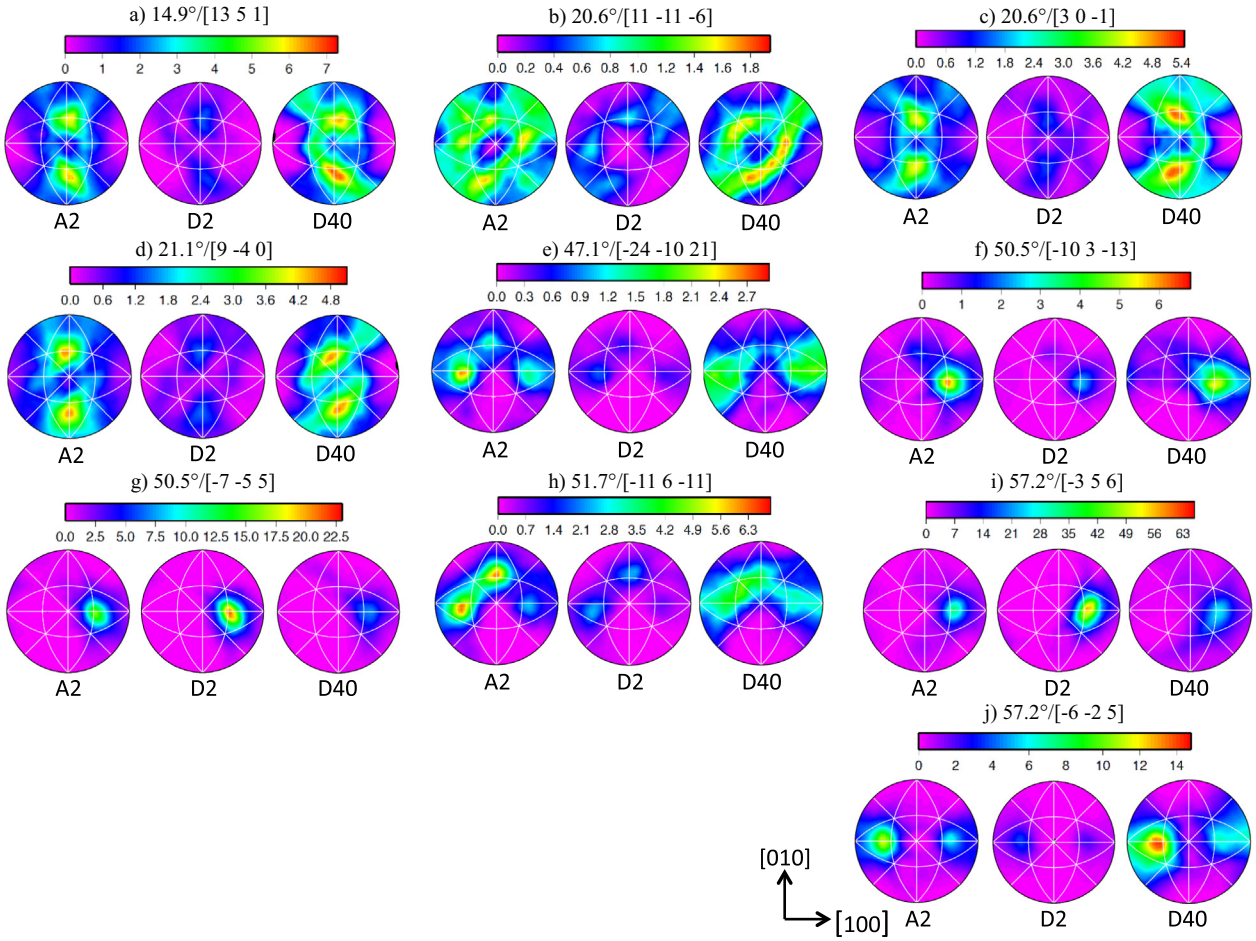

Fig. 16. Distributions of plane normals for boundaries in steels A2, D2 and D40 for different misorientation angles/axes.

60°/[1 1 1], for instance, reveals a maxima centred on the symmetric {1 1 0} tilt boundaries for the current bainitic microstructures (Fig. 14c), rather than {1 1 2} planes observed in the polygonal ferritic microstructures [17,18]. The latter inversely correlated with the distribution of grain boundary energy in a polygonal ferrite, where the {1 1 2} tilt boundaries shows a relatively lesser energy compared with {1 1 0} [18,27]. The present result reveals similar distributions to those recently reported for the lath martensite [19], where the crystallographic constraints associated with the shear transformation (i.e., lath bainite) mainly promotes the {1 1 0} planes during the phase transformation, which may not necessarily be the energetically most favourite configuration.

3.4. Mean spacing of the inter-variant boundary network

To measure the mean spacing of the inter-variant boundary network, the misorientation angle range of 20–40° was firstly excluded from the microstructure as these boundaries were mostly inherited from the prior austenite grain boundaries. Then, the boundaries were filtered as a function of disorientation angle threshold and the mean linear intercept distance between boundaries was measured for all microstructures from the three different heat treatment conditions (Fig. 17a–l). This measurement can be referred to as the mean spacing of {1 1 0} boundary planes as most inter-variant boundaries associated with the Y–K–S condition terminated at or near to {1 1 0} planes (Figs. 14–16). The current result also revealed that the inter-variant boundaries with misorientation axes [1 1 1] and [1 1 0] mainly terminated at {1 1 0} symmetric tilt and {1 1 0} twist plane types, respectively. This ultimately led to measure the mean spacing of inter-variant boundary network of specific {1 1 0} plane type/s (i.e., twist and tilt boundaries, Figs. 17j through k) as a function of disorientation angle for each microstructure. These measurements revealed that the trend of mean spacing of inter-variant boundary network as a function of disorientation angle was qualitatively similar for all microstructures regardless of {1 1 0} plane types (i.e., twist and tilt boundaries, Fig. 17j through k). Initially, the {1 1 0} mean spacing of inter-variant boundary network slightly increased with disorientation angle up to 20° and became nearly constant in a range of 20–40° (i.e., referring to the disorientation angle range originated from the prior austenite grain boundaries) and then increased continuously. In general, the steel D2 microstructure presented a much finer mean spacing of inter-variant boundary network than did the microstructures for steels A2 and D40 (Fig. 17j through k).

The results in Fig. 17 and, in particular in Fig. 17j showing the total results for all boundary types parallel to {1 1 0} planes and all misorientations, are believed to be highly relevant to the question of toughness in the HAZ structures. The {1 1 0} planes in iron are also the planes on which slip takes place. Since the lamellar structure boundaries are to a very high degree aligned along these planes, slip is likely to be favoured along the <1 1 1> directions lying parallel to the laths. Slip distances on other {1 1 0} planes will be restricted by the intersecting lath boundaries. Only 2 of the 12 equivalent {1 1 0}<1 1 1> slip systems benefit from this situation. Since general plasticity requires the activation of 5 independent systems, the relaxation of stresses by plastic yielding at a crack

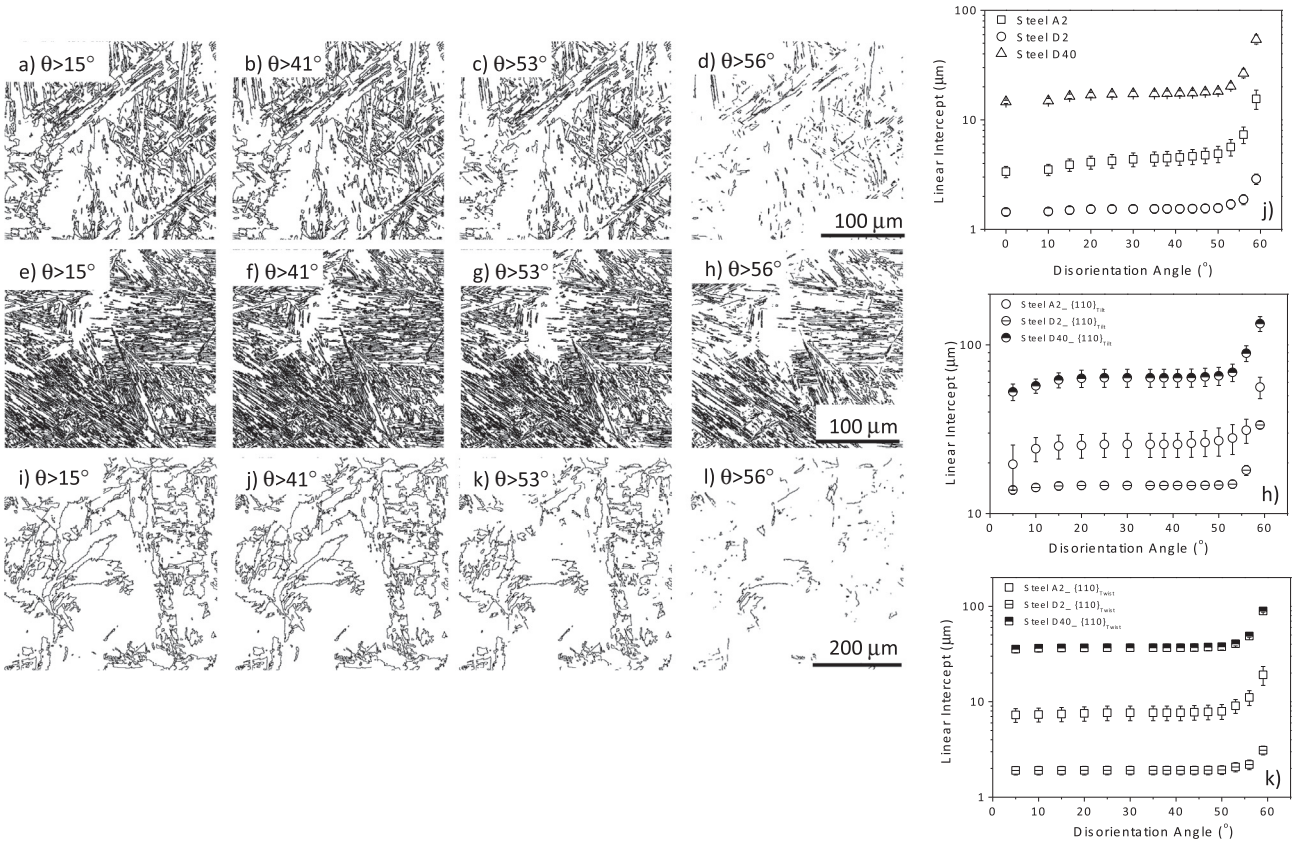

Fig. 17. Thresholded boundary maps for different heat treatment conditions: steel A2 (a–d), steel D2 (e–h) and steel D40 (i–l). Inter-planar spacing of different {1 1 0} boundary plane types for different heat treatment conditions: (j) all types of {1 1 0} planes, (h) {1 1 0} symmetric tilt boundaries and (k) {1 1 0} twist boundaries. θ represents disorientation angle threshold.

tip or defect may be restricted, leading to fracture propagation instead. The degree to which general yielding is inhibited will obviously depend on the spacing between the boundaries that limit the slip length. For the present examples, the mean spacing values for the lath boundaries, including all types of boundary character, are 1.4 μm for steel D2, 3.5 μm for A2 and 13 μm for D40. These rank qualitatively with the impact transition temperatures in Fig. 4 but the dense layers of boundaries in D2 appear to have a particularly strong effect. In support of this hypothesis, it has been observed that similar dense lamellar layers of twins in rolled brass and other fcc metals with low stacking fault energy also restrict slip in an analogous manner, modifying the crystal lattice rotations and the texture that develops [28].

The average thickness of the bainitic laths increases as the cooling is slower and the temperature of the transformation rises. In the case of the Nb-microalloyed steel this has a positive influence on the toughness since the conditions for general yielding become more favourable and the impact transition temperature decreases within the range studied here. Eventually, if the cooling rate becomes sufficiently slow, a change would be expected, leading to a coarse polygonal ferrite with a concomitant rise in the impact transition temperature. For the V–N microalloyed steel A the transformation temperature on cooling is raised significantly (Fig. 6) probably as a result of enhanced ferrite nucleation by VN in the austenite grain boundaries, so that the bainite laths are considerably thicker than in steel D, when compared at the fastest cooling conditions. The resulting microstructure of the V–N steel offers excellent toughness, at least for cooling times $\Delta t_{8/5}$ down to as little as 2 s.

4. Conclusions

The two steels examined here are of comparable strength but respond very differently to heat treatments that simulate conditions in the coarse grained heated affected zones associated with welding. The main difference between the steels is that one (A) was microalloyed with vanadium and nitrogen whereas the other (D) contained niobium. With increasing cooling rate (or decreasing $\Delta t_{8/5}$ from 40 to 2 s) the toughness of the V–N steel increases remarkably with a lowering of the impact transition temperature. In contrast, the Nb steel, which has good toughness after slower cooling, demonstrates a deterioration in its toughness, as a rise in the impact transition temperature.

The fracture properties of the steels after these heat treatments are rationalised in terms of their microstructures. The decrease in toughness for the V–N steel after slow cooling is associated with a raised transformation temperature leading to networks of coarse ferrite grains along the prior austenite grain boundaries, in accordance with earlier observations. The other microstructures which are almost totally bainitic were quantified using a five parameter analysis based on large EBSD data sets. The lath boundaries are dominated by misorientations having <1 1 0> and <1 1 1> rotation axes. However, in both instances the habit planes of the ferrite laths are at or close to {1 1 0}. The inter-lath spacing is significantly larger in the V–N steel than for the Nb steel for the same conditions, which is consistent with a difference of some 80 °C in the transformation temperature measured by dilatometry during cooling. The very narrow laths in the Nb steel are believed to inhibit plastic flow during loading thus limiting plastic relaxation and enhancing its tendency

for fracture. The thicker lath structures in V–N steels are considered to account for their superior toughness in the case of rapid cooling, making these better suited for modern low heat-input welding processes. The approach used here demonstrates the power of the five parameter analysis of grain boundaries and its potential for solving problems of a technological nature.

Acknowledgements

The authors thank Vanitec for financial support as well as the Australian Research Council for the work at Deakin University. Particular thanks go to David Milbourn and Peter Hodgson for their support and to colleagues Eva Lindh-Ulmgren, Karl Fahlström and Tadeusz Siwecki for advice and assistance. A part of this work was carried out with the support of the Deakin Advanced Characterisation Facility.

Appendix A

The TSL software was employed to post process the EBSD maps for the plane character distribution analysis and mean spacing of inter-variant boundary network measurement. Briefly, a grain dilation clean-up function was first used to all orientation maps to remove uncertain data. A single orientation was then assigned to a given grain by averaging all orientation data belonging to that grain (hereafter called the cleaned EBSD map). To measure the five-parameter boundary character distribution, the line traces/segments were extracted from the cleaned EBSD maps after smoothing uneven grain boundaries by the reconstruct grain boundaries function in the TSL software, using a boundary deviation limit of 2 pixels (i.e., 0.4 μm).

To measure mean spacing of the inter-variant boundary, the cleaned EBSD maps collected on a hexagonal grid were converted to a square grid pattern. They were then calculated as a disorientation map, where each pixel has the value of the minimum disorientation angle between that pixel and its eight nearest neighbours in the EBSD map. The mean spacing of boundary network structure at different disorientation angle thresholds and misorientation axes was determined as an average of the mean linear intercepts measured in the horizontal and vertical directions.

References

[1] P.H.M. Hart, Welding Cutting 88 (2003) 204.
[2] S. Kanazawa, A. Nakashima, K. Okamoto, K. Kanaya, Tetsu-to-Hagané 61 (1975) 2589.
[3] Hannerz NE. Proc Conf. Welding of HSLA (Microalloyed) Structural Steels, Rome (1976) pp. 365–385.
[4] MNC Handbook nr. 15 Welding of Steels, SIS, 1986.
[5] P. Kah, J. Martikainen, Rev. Adv. Mater. Sci. 30 (2012) 189.
[6] S.A. David (Ed.), Proceedings Trends in Welding Research, ASM International, 2012.
[7] Lagneborg R, Hutchinson B, Siwecki T, Zajac S. The role of vanadium in microalloyed steels, ISBN 978-91-633-9359-4 Distr. www.Vanitec.org. publications.
[8] N.E. Hannerz, B.M. Jonsson-Holmqvist, Metal Sci. 8 (1974) 228–234.
[9] Zajac S, Siwecki T, Hutchinson B, Svensson L-E, Attlegård M. Swedish Institute for Metals Research, Internal Report IM-2764, 1991.
[10] S. Zajac, T. Siwecki, L.-E. Svensson, Int Symp On Low Carbon Steels, TSM, Pittsburgh, USA, 1993. pp. 511-523.
[11] P.S. Mitchell, P.H.M. Hart, W.B. Morrison, in: M. Korchynsky et al. (Eds.), Microalloying 9, I&SS, Pittsburgh, USA, 1995, pp. 149–162.
[12] G.S. Rohrer, D.M. Saylor, B. El Dasher, B.L. Adams, A.D. Rollett, P. Wynblatt, Z. Metallkd. 95 (2004) 197.
[13] B. Pawlowski, Achiev. Metal Manufact. Eng. 49 (2011) 331.
[14] C. Garcia-Mateo, C. Capdevilla, F.G. Caballero, C. Garcia de Andrés, ISIJ Int. 48 (2008) 1270–1275.
[15] T. Furuhara, J. Yamagushi, N. Sugita, G. Miyamoto, T. Maki, ISIJ Int. 43 (2003) 1630–1639.
[16] K. Zhu, H. Chen, J.-P. Masse, O. Bouaziz, G. Gachet, Acta. Mater. 61 (2013) 6025.
[17] H. Beladi, G.S. Rohrer, Metall. Mater. Trans. A 44 (2013) 115.
[18] H. Beladi, G.S. Rohrer, Acta Mater. 61 (2013) 1404.
[19] H. Beladi, G.S. Rohrer, A.D. Rollett, V. Tari, P.D. Hodgson, Acta Mater. 63 (2014) 86–98.
[20] H. Beladi, N.T. Nuhfer, G.S. Rohrer, Acta Mater. 70 (2014) 281–289.
[21] D.M. Saylor, B.S. El Dasher, T. Sano, G.S. Rohrer, J. Am. Ceram. Soc. 87 (2004) 670–676.
[22] D.M. Saylor, B.S. El Dasher, Y. Pang, H.M. Miller, P. Wynblatt, A.D. Rollett, G.S. Rohrer, J. Am. Ceram. Soc. 87 (2004) 724–726.
[23] C.S. Roberts, J. Metals 5 (1953) 203.
[24] J. Young, Proc. R. Soc. London 112A (1926) 630–641.
[25] G. Kurdjumov, G. Sachs, Z. Phys. 48 (1930) 325–343.
[26] K. Glowinski, A. Morawiec, J. Mater. Sci. 49 (2014) 3936–3942.
[27] S. Ratanaphan, D.L. Olmsted, V.V. Bulatov, E.A. Holm, A.D. Rollett, G.S. Rohrer, Acta Mater. 88 (2015) 346–354.
[28] W.B. Hutchinson, B.J. Duggan, M. Hatherly, Metals Technol. 9 (1979) 398.